

Chapter 11

Semiconductor Nanowires for Solar Cells

S.T. Picraux, J. Yoo, I.H. Campbell, S.A. Dayeh, and D.E. Perea

Abstract This chapter discusses studies of semiconducting nanowire arrays for solar cells. The concept of 3D nanowire architectures for photovoltaic light harvesting to effectively decouple light absorption and carrier separation is presented. The available literature on semiconductor nanowire solar cell studies is summarized. Optical and electronic aspects specific to nanowires are discussed to illustrate the basic principles. Finally, issues related to integration for solar cell applications are highlighted.

11.1 Introduction

Nanoscale semiconductor materials have received great interest in recent years for their potential applications to solar energy harvesting. The primary motivation for this explosion of interest has been the ability to tailor materials properties at the nanoscale through size and structure in ways not possible at the macroscale. Key aspects being exploited are (1) nanostructuring to enhance the scattering, local field, absorption, and conversion of photons across the solar spectrum to generate charge carriers, and (2) nanoscale device designs to efficiently harvest the charge carriers for electrical energy generation or chemical fuel production. Areas of current research attention include arrays of radial junction nanowires to enhance photon absorption and provide efficient carrier collection [1], nanoparticle multi-exciton effects to create more than one electron–hole pair per absorbed photon [2,3], and mesoporous materials to enhance photochemical conversion in dye-sensitized solar cells [4]. In addition to the potential advantages of providing enhanced

S.T. Picraux (✉) · J. Yoo · I.H. Campbell · S.A. Dayeh · D.E. Perea
Center for Integrated Nanotechnologies, Los Alamos National Laboratory, Los Alamos,
NM 87545, USA
e-mail: picraux@lanl.gov; trip297@gmail.com; campbell@lanl.gov; shadi@lanl.gov;
d-perea@lanl.gov

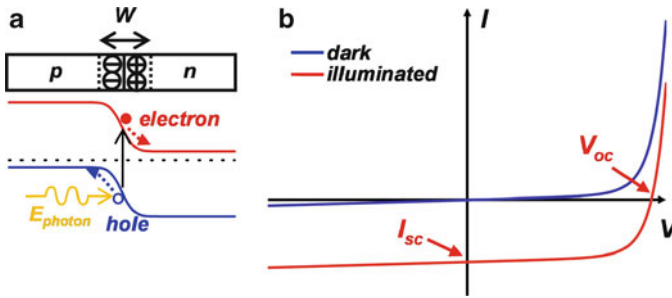


Fig. 11.1 (a) *Top* is schematic of a p–n junction showing depletion region (W) with ionized charges; *bottom* is the correspondent energy–band diagram. Incident light creates an electron–hole pair that is field swept to the charge–neutral regions. (b) Typical photodiode I – V characteristics under dark and illumination conditions

photon absorption, carrier generation, and carrier collection, nanoscale materials can be configured into more complex architectures, and synthesized directly on or transferred to low-cost substrates. In this chapter, we focus on nanowire solar cells. These structures comprise vertical arrays of semiconducting, coaxial p–n junction nanowires. The wires have typical diameters ranging from ~ 100 nm to ~ 2 μm ; since they span the nano- to micrometer size range they are variously referred to as wires, pillars, nanowires, and microwires. Here, for simplicity, we exclusively use the term nanowires (NWs).

The solar cell principle, as illustrated in Fig. 11.1, is based on an unbiased p–n junction photodiode connected to a load impedance to generate power [5]. There is a region of high electric field, called the depletion region (labeled W), at the junction of the p- and n-type semiconductors where photogenerated electrons and holes are separated by the electric field, producing a current. In addition, carriers generated in either the p- or n-type material within a minority charge carrier diffusion length of the depletion region can be collected at the junction and contribute to the total current. Key criteria for effective solar cells are high absorption of the incident light in the active region of carrier collection and minimal loss of carriers due to recombination. Conventional crystalline silicon solar cells, as illustrated in Fig. 11.2a, rely primarily on thick diffusion regions (~ 200 – 250 μm), compared to the much thinner drift region, for carrier collection. This approach is due to the weak absorption of light by Si across the solar spectrum, necessitating a substantial thickness of Si to absorb the incident light. Thus, high-efficiency Si solar cells require very high-quality, defect-free material with large carrier mobilities and long carrier lifetimes. The current record efficiency under terrestrial illumination conditions for a Si cell is 25%, which is a significant fraction of the Shockley–Queisser limit of $\sim 31\%$ for single junction cells and was achieved over a decade ago [6]. For multijunction tandem cells composed of two or more different stacked semiconductors, the record is 42.8% (for Si/GaAs/GaInP) [6]. However, the manufacturing costs are high for such record efficiencies and commercial Si solar cells at the module level typically range from ~ 15 to 22% [7].

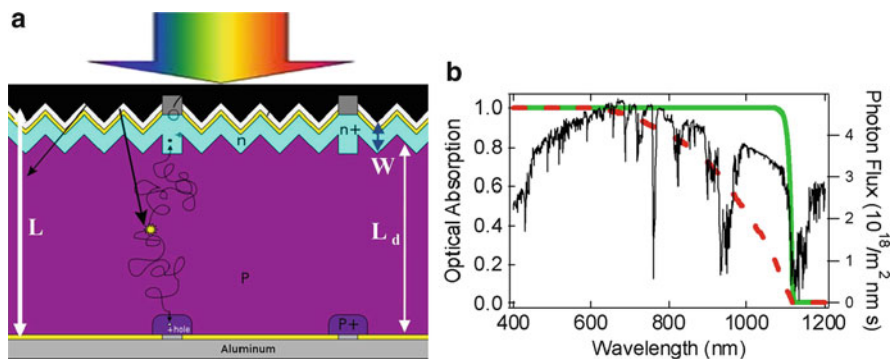


Fig. 11.2 (a) Schematic of a conventional Si solar cell with antireflection coating and surface texturing. Typical cell thickness, $L \sim 200 \mu\text{m}$, is used to absorb the light; carrier collection is primarily from the diffusion region (L_d) where $L_d \gg W$, the junction drift region. (b) Solar intensity spectrum (black curve) and the relative absorption for a $5 \mu\text{m}$ thick Si slab (red dashed line) and an array of $5 \mu\text{m}$ long Si NWs (green line)

The potential for improved performance and cost reductions of NW arrays over their bulk photovoltaic counterparts is primarily due to (1) increased absorption due to diffuse light scattering in NW arrays, (2) short collection lengths of minority carriers that are radially separated and collected normal to the light absorption direction, and (3) flexibility of cell integration on a variety of low-cost carrier substrates. A key point is that single-crystalline NWs can be grown by the vapor–liquid–solid (VLS) method, a process comparable to thin-film growth technology. In crystalline Si cells, the Si ingot growth and slicing account for up to 50% of the overall cost of wafer-Si cells. In contrast, thin-film solar cells are attractive due to their potential for reduced costs. However, after many years they continue to have limited cell efficiencies due to grain boundary and related carrier recombination loss issues. For example, for amorphous Si cells the highest reported efficiency is 10% [6]. Both CdTe and CIGS (CuInGaSe_2) thin-film cells have demonstrated higher efficiencies, but materials availability may limit their large-scale use.

With nanostructured 1D materials it is possible to achieve thin layers of single-crystal NWs grown on or transferred to low-cost substrates. Thus, a NW approach uses less high purity Si ($\sim 1/10$) along with lower cost materials growth and device fabrication techniques. Although improvements in efficiency over conventional crystalline silicon solar cells are not anticipated, achieving reasonably good efficiencies ($\sim 15\text{--}20\%$) in combination with low-cost thin-film processing could dramatically impact the application of solar cells. Figure 11.3 illustrates this point by comparing the leveled cost of energy (LCOE) using the National Renewable Energy Laboratory “Solar Advisor Model” [8] vs. efficiency for several commercial crystalline Si and thin-film solar cells in comparison to estimated values that might be anticipated if a successful Si NW solar cell approach were achieved (P. Schuele, D. Evans, Sharp Laboratories of America, private communication).

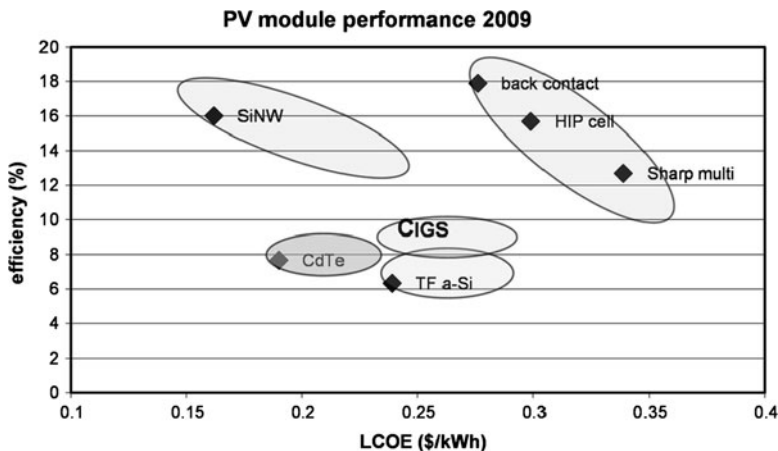


Fig. 11.3 Comparison of the levelized cost of energy model values of 2009 photovoltaic modules for several commercial Si crystalline cells (SunPower SPR-220 back contact and Sanyo HIP-190DA1 monocrystalline, and Sharp 165U1 multicrystalline) along with amorphous Si (Unisolar US64), CdTe, and CIGS thin-film cells to an estimated potential value for Si NW cells (P. Schuele, D. Evans, Sharp Laboratories of America, private communication)

11.2 Key Concepts

The orthogonalization of the light absorption and carrier collection directions is a key aspect of the radial p–n junction NW photovoltaic (PV) cell concept (Fig. 11.4). This approach is dependent on realizing three-dimensional (3D) structures. In 1994, a group at the University of New South Wales (UNSW) suggested the architecture of a parallel multijunction PV cell consisting of multilayered p–n junctions and metalized grooves [9]. The UNSW approach was to use the 3D structured cell to attain close to 100% carrier collection efficiency by dividing the PV cell into segments. Additionally, a 3D structure consisting of many etched Si stripes could provide photon recycling due to increased effective cell thickness [10]. In each Si stripe, light absorption occurs along the vertical direction, while the photogenerated carriers are extracted through the sidewalls of the Si stripe. In practice, the 3D structured PV cell based on etched Si stripes demonstrated up to 18.5% efficiency with production costs similar to surface textured Si solar cells. However, in bulk and thin-film PV cell research, the 3D structured PV cell has not been a major focus because of the difficulty of concurrent achievement of carrier loss minimization and light absorption maximization.

A radial p–n junction in an NW array architecture is an ideal structure for highly efficient p–n junction solar cells. The radial geometry of the p–n junction allows for the orthogonalization of the light absorption and carrier collection directions. In bulk and thin-film PV cells, the fabrication of radial or surrounding p–n junctions is not easily achieved, and requires micromachining processes, which increase production

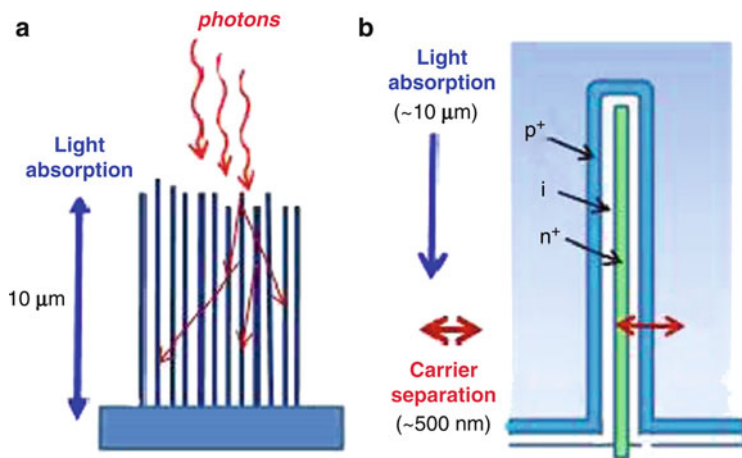


Fig. 11.4 (a) Diffuse scattering of photons by Si NWs greatly reduces vertical distance for light absorption. (b) Radial p-i-n NW junction for carrier separation and collection through substrate and top transparent contact

costs. Semiconductor NWs provide a suitable material system for radial p-n junction PV cells because as-grown semiconductor NWs are ready for radial p-n junctions. Furthermore, semiconductor NWs can overcome material compatibility issues critical to thin-film PV cells. For example, mismatches of thermal expansion coefficients and lattice constants between the substrate and thin films over large areas lead to stresses, whereas single-crystal semiconductor NWs can be prepared on various substrates by diverse methods with minimal accumulated stress. Minority carrier diffusion lengths (L_{diff}), an important material characteristic in determining solar cell efficiency, are in the range of ~ 100 s of nanometers to several micrometers in thin films because they are limited by grain sizes, whereas values of L_{diff} in single-crystalline Si NWs have been reported in the range of 2 to $> 20\ \mu\text{m}$.

The orthogonalization through 1D nanostructuring is a key factor in the NW approach to solar cells where the optical absorption and charge collection constraints are decoupled. In conventional crystalline silicon solar cells, a basic problem is that the optical absorption is weak. As a result thick Si regions are required to absorb the incident light and charge carrier generation occurs throughout the region (Fig. 11.2a). Thus, minority charge carriers must be transported by diffusion over large distances without recombination, necessitating the use of essentially perfect single-crystal materials. For example, for the highest silicon solar cell efficiencies $\sim 260\ \mu\text{m}$ thick region of high-quality single-crystal Si wafer is required. In contrast, crystalline Si NW arrays can absorb the light in $\sim 10\ \mu\text{m}$ and simultaneously allow independent control over the charge carrier separation (Fig. 11.4). The first key difference is that the light collection takes advantage of the diffuse scattering of photons by the NWs due to the dielectric constant difference with the surrounding medium to allow complete absorption and carrier excitation within a depth of

$\leq 10 \mu\text{m}$. The second key difference is that rapid carrier separation ($\leq \text{ns}$) occurs by drift in the high electric field region within the radial p–n junction with distances of $\sim 1 \mu\text{m}$ for the carriers to be collected by the single-crystal NW conducting core and shell. This contrasts to the process in conventional solar cells where slow carrier separation ($\sim \mu\text{s}$) occurs by diffusion with carriers collected over distances of $\geq 100 \mu\text{m}$, requiring the absence of recombination centers (or charge traps) over these large distances. As a result the carrier collection times are dramatically reduced in NWs, from μs to ps, facilitating efficient charge collection.

The unique structure of the NW solar cell allows one to maximize the effective width of the depletion region and collect the carriers absorbed in the n- and p-type regions. In bulk silicon solar cells, the depletion region is $< 10 \mu\text{m}$ as limited by the energy gap of the material and residual doping levels. Since $\sim 200 \mu\text{m}$ of Si is required to absorb the light efficiently, the depletion region is only $\sim 5\%$ of the absorbing volume. In contrast, in the NW structures the amount of Si required is much smaller and the depletion region can be made to be a large volume fraction, $\sim 50\%$, of the semiconductor carrier collection region. Similarly, because of the nanostructure design, the p, n, and any intrinsic regions are relatively thin in the radial direction, and carriers with effective minority carrier diffusion lengths of the order of $\sim 1 \mu\text{m}$ will be effectively collected. This means the Si NWs could still function effectively with mobility-lifetime ($\mu\tau$) products four orders of magnitude smaller (lower quality material) than conventional Si solar cells. In addition to maximizing photon collection, the diode series resistance and defect-related surface states need to be minimized. Similar to bulk solar cells the series resistance can be made small by increasing the doping and size of the core and outer shell p+ and n+ regions. An important issue is that surface and interface states can act as recombination centers and reduce charge carrier collection. The adverse effects of such states must be minimized for these nanoscale architectures if acceptable efficiencies are to be achieved. Preliminary results, as summarized in Sect. 11.4, provide initial evidence for the benefits of NW array solar cells and highlight the need to develop methods to produce high performance, single-crystal p–i–n NW devices.

11.3 Nanowire Fabrication

The NW solar cell concept emerged from recent experience in the growth of semiconducting NWs by bottom-up techniques. The VLS technique, while first reported almost a half century ago [11], provides good control of bottom-up NW growth, and has been studied intensively over the last decade. VLS growth has become the preferred method for NW fabrication because it provides a versatile method to grow single-crystal wires of Si and other semiconductors based on chemical vapor deposition (CVD) methods [12]. Further, this growth method does not require crystalline substrates to achieve good single-crystal NWs. However, the NWs are randomly tilted when grown from a noncrystalline substrate, whereas

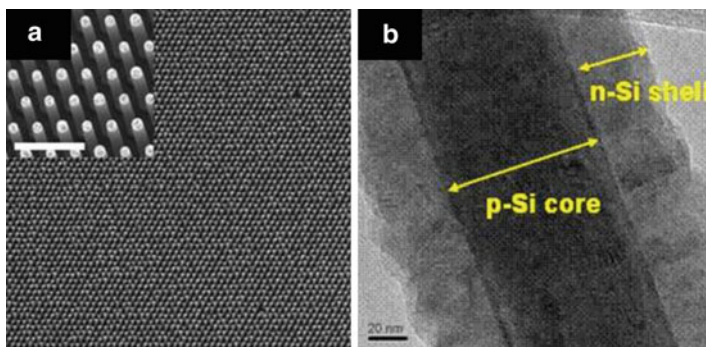


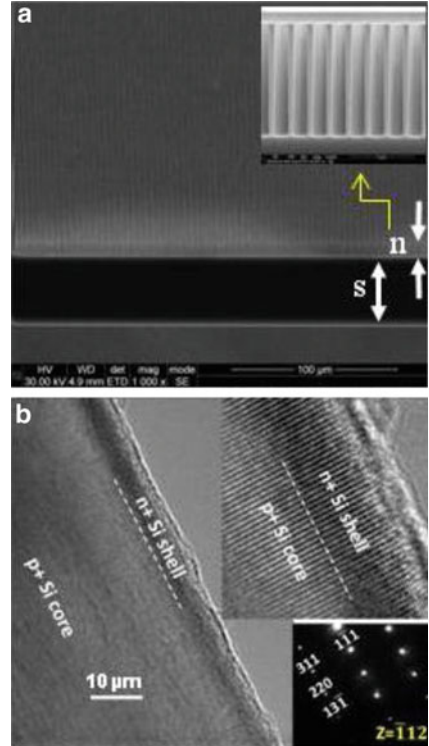
Fig. 11.5 (a) Lithographically patterned $400 \times 400 \mu\text{m}$ VLS-grown Si NW array with diffused P shell on Si(111) substrate. *Inset* shows enlargement of $2.6 \mu\text{m}$ diameter NWs; *scale bar*: $20 \mu\text{m}$ [13]. (b) TEM image of Si NW with diffused shell; *scale bar*: 20nm (image courtesy of Dr. Qi. Li and Prof. E.C. Dickey, www.personal.psu.edu/jmr31/index_files/Page1004.htm)

regular vertical arrays can be achieved generally for larger diameter NWs grown from crystalline Si(111) substrates. VLS growth proceeds from the substrate via a metal-catalyzed nanoparticle seed. Gold is most frequently used as the catalyst with either SiH_4 at temperatures $\sim 500^\circ\text{C}$ or SiCl_4 at temperatures of $\sim 1,000^\circ\text{C}$ used as the source gases. Figure 11.5a shows an array of Si NWs where the growth seeds were lithographically patterned to achieve a regular array [14]. In this case, the n-type shell was formed by P diffusion subsequent to SiCl_4 NW growth after removal of the Au growth seed. Cu has also been recently used as the growth catalyst, with improvements in the minority carrier diffusion lengths being reported for SiCl_4 growth [13]. To better understand the ultimate limits of efficiency for NW solar cells, the present authors have prepared Si NWs by a metal-free, top-down Bosch reactive ion etch process. Figure 11.6a shows a Si NW array on a thin Si substrate. Unlike other reports, these studies have achieved single-crystalline radial n^+ shell grown directly on the NWs by a vapor–solid method using SiH_4 and PH_3 precursors as demonstrated in Fig. 11.6b. Compound semiconductor NWs can also be grown by the bottom-up VLS process and radial vapor–solid shells have been grown. While improvements in the various processing steps for NW growth and radial junction formation are still needed for solar cell applications, the fabrication methods are encouraging.

11.4 Overview of Nanowire Solar Cell Studies

Despite the described advantages of using semiconducting NWs for solar cells, research on semiconductor NWs and semiconductor-based photovoltaics was essentially conducted separately until recently. Many researchers have addressed challenges related to NW materials science and device fabrication, including doping, axial, and radial heterostructure formation, electrical contact formation,

Fig. 11.6 (a) SEM tilted view of a large area top-down fabricated array of $10\ \mu\text{m}$ tall Si NWs (n) on $40\ \mu\text{m}$ thick Si substrate (s); *inset* shows close-up of Bosch-etched $500\ \text{nm}$ diameter Si nanopillars. (b) TEM image of a single-crystalline epitaxial radial shell on a Si NW formed by vapor–solid growth of P-doped Si; *inset* shows HRTEM lattice image of the p+ core to n+ shell region and corresponding diffraction pattern



and integration of NWs on various substrates. These efforts have opened up opportunities for the realization of radial p–n junction PV cells. Research on semiconductor NW solar cells first received attention in 2005 when a group from Caltech published a paper that discussed important device physics aspects of a radial p–n junction nanorod geometry for efficient, low-cost solar cells [15]. In this paper, the authors formulated the advantages of radial p–n junctions compared to planar p–n junctions based on simultaneous maximization of light absorption and carrier collection through separation of the light absorption direction and carrier collection direction, and supported the proposed benefits with a model. The enhanced light absorption in Si NW arrays was formulated later by a group from MIT in 2007 [16], and has since been confirmed by many researchers [17–19]. A group from GE provided among the earliest demonstrations of Si NW solar cell operation using VLS growth of arrays of crystalline Si NW cores on metal foil followed by a radial shell of amorphous Si (a-Si) [20]. A Harvard group provided an early demonstration of the PV properties of single Si radial p–n and p–i–n junction NW solar cells [21].

Since 2007, the performance characteristics of radial NW p–n junction solar cells have been reported for various fabrication approaches as summarized in Table 11.1 for Si and Table 11.2 for compound semiconductors. In these tables, the experimental results are classified by material preparation process. The NW

Table 11.1 Measured properties of Si nanowire-based photovoltaic cell

Nanostructure formation	Radial p-n junction formation	Structure	Efficiency (%)	V_{oc} (V)	J_{sc} (mA/cm ²)	FF	References
VLS	Amorphous Si	ITO/n-type <i>a</i> -Si shell/p-Si NWs on metal foil	0.1	0.13	–	0.28	[20] – GE, USA (2007)
		n ⁺ -Si/i-a-Si/i-Si NWs on glass		0.24	2.6	0.41	[22] – Ecole Polytechnique, France (2010)
	Polycrystalline Si	Single n-Si/i-Si/p-Si NW	3.4	0.26	$I_{sc} = 0.503$ nA	0.55	[21] – Harvard U., USA (2007)
		Al ₂ O ₃ /p-Si shell/n-Si NWs on n-Si, back contact	1.8	0.28	18	–	[23] – IBM, USA (2009)
		n-Si/p-Si NWs on p-Si	1.8	0.29	11	0.56	[24] – Penn. State U., USA (2010)
	Diffusion	n-Si shell/p-Si microwires on p-Si (p- and n-layers separated by oxide)	7.9	0.5	24	>0.65	[25] – Caltech, USA (2010)
		n-Si shell/p-Si microwires on p-Si	2.3	0.5	7.6	0.57	[13] – Penn. State U., USA (2010)
		Single silicon nitride/n-Si shell/p-Si microwires on p-Si (111)	9	0.54	23	0.75	[26] – Caltech, USA (2011)

(continued)

Table 11.1 (continued)

Nanostructure formation	Radial p-n junction formation	Structure	Efficiency (%)	V_{oc} (V)	J_{sc} (mA/cm ²)	FF	References
Dry etching	Amorphous Si	ITO/n-i-p <i>a</i> -Si/Ti/AuAg/etched and tapered Si nanopillars	8.2	0.89	13.9	0.66	[27] – Boston U./Solasta, USA (2010)
	Ion implantation	p-Si shell/n-Si conical-frustrum array on n-Si	10.8	0.59	26.4	0.69	[28] – Cornell U., USA (2010)
	Diffusion	p-Si shell/n-Si nanopillars	5.3	0.52	16.8	0.61	[19] – U. C. Berkeley, USA (2010)
		n-Si shell/p-Si nanopillars	8.7	0.56	20	0.78	[29] – Penn. State U., USA (2010)
Wet etching	Polycrystalline Si	p-Si shell/n-Si NWs	0.46	0.29	4.3	0.33	[30] – U. C. Berkeley, USA (2008)
	Diffusion	n-Si shell/p-Si NWs on p-Si	7.19	0.5	20.6	0.70	[31] – Hanyang U., Republic of Korea (2010)
		n-Si shell/p-Si NWs on p-Si	1.47	0.45	6.3	0.53	[32] – NTU, Singapore (2010)
Conventional crystalline Si	Highest confirmed	Conventional cell	25.0	0.706	42.7	0.882	[6]
Conventional amorphous Si	Highest confirmed	Conventional cell	10.1	0.886	16.75	0.67	[6]

Table 11.2 Measured properties of compound semiconductor nanowire-based photovoltaic cell

Nanostructure formation (Material)	Radial p-n junction formation	Structure	Efficiency (%)	V_{oc} (V)	J_{sc} (mA/cm ²)	FF	References
VLS (GaAs)	Epitaxial grown (GaAs)	ITO/p-GaAs/n-GaAs NWs on n-GaAs(111)B Single n-GaAs/n-GaAs/p-GaAs NW ITO/SiO ₂ /p-GaAs shell/n-GaAs NWs on n-GaAs substrate	0.83 4.5 1.09	~0.2 0.14	$I_{sc} = 0.2$ mA $I_{sc} = 0.36$ mA	0.27 0.27	[33] – McMaster U., Canada (2009) [34] – EPFL, Switzerland (2009) [35] – McMaster U., Canada (2011)
VLS (GaN)	Epitaxial grown (GaN)	Single p-GaN/InGaN/n-GaN NW	0.25	1.0	$I_{sc} = 58$ pA	0.56	[36] – Harvard U., USA (2009)
Electrodeposition (ZnO)	Electrodeposition (Cu ₂ O)	Au or Ag/p-Cu ₂ O/n-ZnO NW/ITO	0.47	0.28	4.4	0.39	[37] – Ludwig-Maximilians U., Germany/U. Cambridge, UK (2010)
Solution grown (ZnO)	Solution grown (Cu ₂ O)	Au or Al/p-Cu ₂ O NPs/n-ZnO NW/ITO	0.053	0.15	1.43	0.25	[38] – UC Berkeley, USA (2009)
VLS (CdS)	Thermal evaporation (CdTe)	Au/Cu/p-CdTe/n-CdS NW/Al	5.8	0.62	21	0.42	[39] – UC Berkeley/LBL, USA (2009)
ELCD (CdS)		Graphite/Cu/p-CdTe/n-CdS NW/ITO	6.5	0.71	25.3	0.36	[40] – U Kentucky, USA (2011)
Anodization (TiO ₂)	Electrodeposition (Cu ₂ O)	Au/p-Cu ₂ O shell/n-TiO ₂ nanotube/Ti foil	~0.01	0.25	0.33	0.27	[41] – UCLA, USA (2011)

formation process can be divided into bottom-up VLS growth and top-down dry or wet etching methods. For Si, the radial NW p–n junctions have been formed by dopant diffusion or vapor deposition, whereas cells with single-crystalline shells grown on NW cores have not been reported. To date, published results have reported NW solar cells with either diffused dopants to form single-crystalline radial shells on crystalline core or deposited vapor–solid amorphous or polycrystalline shells [20–23, 27, 30]. For compound semiconductor NWs, a variety of methods have been used to obtain doped shells including ion implantation, diffusion, and MBE [13, 19, 25, 26, 31, 32], with single-crystal core/shell structures demonstrated for GaN/InGaN [36].

In spite of the predicted advantages, NW radial p–n junction solar cell devices initially gave low efficiencies (<1%). The low efficiencies indicated that there are still many unresolved issues such as obtaining high-quality shell formation, reducing interfacial carrier recombination loss due to the large NW surface-to-volume ratio, and forming conformal transparent electrodes on the surface of radial p–n junction structures with low specific contact resistance. To resolve these issues, researchers have achieved increasingly improved crystalline shells by diffusion and ion implantation, surface passivation by dielectrics, and deposition of transparent conducting oxide as an electrode layer. These results are summarized in Table 11.1 for Si NWs, with several NW radial p–n junction Si solar cells having exhibited efficiencies in the range of 5–10%. These efficiency values are still far from those of conventional crystalline Si solar cells (see Table 11.1), but larger than that of other NW-based solar cell approaches, such as hybrid and dye-sensitized cells [42, 43].

Semiconductor NW radial p–n junction PV cells still have much room for improvement in their device performance. The process of improving device performance will help to clarify important issues in both the science and technology of nanoscale structures, both of which are closely related to fundamental understanding of how fabrication processes affect materials characteristics. On the science side, NW radial p–n junctions provide a novel platform to investigate carrier transport and photon management, as discussed in the following sections. One important material parameter for PV devices is the effective minority carrier diffusion length, and the values reported for Si NWs to date are summarized in Table 11.3 along with bulk values for Si at comparable doping levels. These effective diffusion lengths have been measured by electron beam induced current (EBIC) and scanning photocurrent microscopy (SPCM) techniques with the studies primarily conducted for axial NW junction configurations. Since the NW surface provides a favorable site for carrier recombination, it is useful to compare the measured effective diffusion length to the NW diameter. From Table 11.3, these ratios are seen to vary from ~ 1 to 30. It is generally observed that these effective diffusion lengths are much lower than their bulk counterparts, but exact diameter dependences cannot be concluded at this time given the different doping levels and limited results. Maintaining relatively long diffusion lengths for the p–n junction NWs in solar cells will be important if reasonable efficiencies are to be achieved. In the following sections, insight into the various fundamental materials issues is discussed. Technologically, NW radial p–n

Table 11.3 Measured effective minority carrier diffusion lengths for nanowires

Material	Structure	Method	$N_A(\text{cm}^{-3})$	$N_D(\text{cm}^{-3})$	d (nm)	ℓ_p (nm)	ℓ_p/d	ℓ_n (nm)	ℓ_n/d	References
NW (Si)	Au/n-Si/Au	EBIC	-	$\sim 1 \times 10^{19}$	30-100	20-80	~ 1	-	-	[44] - Northwestern U., USA (2008)
	Al/n-Si/Al Schottky	SPCM	-	$1 - 10 \times 10^{17}$	900	2,200	~ 2.3	-	-	[45] - Caltech, USA (2008)
	Al/p-Si/n-Si/Al Diffused radial p-n junctions	SPCM	-	$\sim 1 \times 10^{17}$	$\sim 1,500$	-	-	$> 20,000$	> 13	[26] - Caltech, USA (2011)
	Ni/n-Si/p-Si/Ni VLS axial p-n junctions	SPCM	2×10^{16}	2×10^{18}	80	660	~ 8	980	~ 12	A. Mohite et al. (in preparation) Los Alamos Natl. Lab., USA
NW (CdS)	Ti/i-CdS/Ti Schottky	SPCM	-	-	50	650	~ 10	1,470	~ 30	[46] - Northwestern U., USA (2006)
Bulk	Si	-	1×10^{17}	1×10^{17}	-	70,000	-	200,000	-	[47]
Bulk	Si	-	1×10^{18}	1×10^{18}	-	20,000	-	40,000	-	[47]
Bulk	Si	-	1×10^{19}	1×10^{19}	-	2,000	-	4,000	-	[47]

junction cell processing also presents many challenging issues, including large-scale processing, integration onto various substrates, small sizes, and highly sensitive surfaces. Integration of NW-based PV cells onto flexible substrates is a particularly important issue for the eventual achievement of highly efficient, low-cost solar cells and this area is discussed briefly at the end of the chapter.

11.5 Enhanced Optical Absorption in Nanowire Arrays

An efficient solar cell must absorb essentially all of the solar radiation above its energy gap and collect all the photogenerated charges. Increasing the effective optical absorption of the solar cell material allows one to use less and/or lower quality material. Less material can be used because the photons will be absorbed in a smaller volume. The resulting photogenerated charges are easier to collect because they are created closer to the device electrodes. Therefore, lower quality material with poorer charge collection properties, e.g., relatively small minority carrier diffusion lengths, can efficiently collect the charge. Using less and/or lower quality material decreases the absorbing layer cost which can be beneficial if these savings exceed the costs of the additional processing and materials used to increase the optical absorption.

The relative utility of using NWs to enhance light absorption depends significantly on the material being used. The most important material parameter is the optical absorption depth for the wavelengths of light in the solar spectrum (Fig. 11.2b). The smaller the absorption depth the less material is required to absorb the photons in a simple thin-film structure. Figure 11.7 shows the optical absorption depth as a function of wavelength for three representative solar cell materials: cadmium telluride (CdTe), gallium arsenide (GaAs), and crystalline

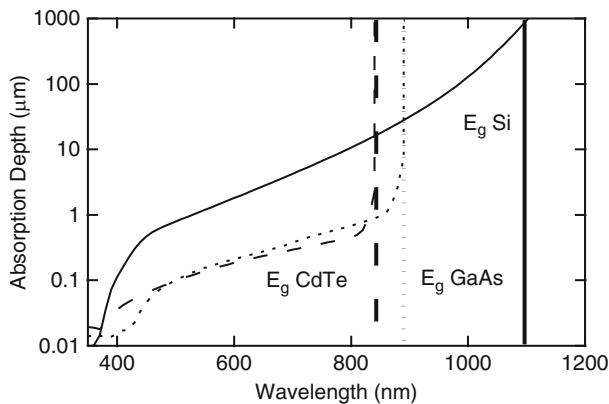


Fig. 11.7 Absorption depth as a function of wavelength for CdTe, GaAs, and crystalline Si. The energy gaps of each material are indicated by *vertical lines*

silicon (c-Si). Cadmium telluride is becoming the dominant thin-film solar material and GaAs is widely used in expensive, high-efficiency solar cells. Crystalline silicon is the dominant solar cell material accounting for $\sim 90\%$ of the world's solar cell production. Cadmium telluride and GaAs have direct band gaps of ~ 1.5 eV (830 nm) and ~ 1.42 eV (875 nm), respectively, and silicon has an indirect band gap of ~ 1.12 eV (1,100 nm). For CdTe and GaAs, the absorption depths are < 1 μm for all wavelengths from 350 nm to nearly their band gaps. In contrast, the absorption depth of Si is > 1 μm for all wavelengths longer than ~ 550 nm and exceeds a depth of 100 μm for wavelengths up to ~ 100 nm above the energy gap. Because of this two orders of magnitude difference in absorption depth, most NW solar efforts are being focused on c-Si structures. Crystalline silicon NW structures have the potential to use both significantly less and lower quality material.

The effective absorption of solar cell material can be increased by three basic approaches: (1) decreasing the reflection of incident light; (2) increasing the optical path length in the material; and (3) increasing the optical intensity in the material. In many cases, the same physical structure produces combinations of these effects simultaneously. Conventional c-Si cells utilize antireflection (AR) coatings and surface texturing to decrease the reflection and increase the effective optical path length in the absorbing silicon layer [48]. A typical AR coating is a double layer MgF_2/ZnS thin-film structure [49]. The average reflectance from the AR-coated textured surface over the relevant 350–1,100 nm wavelength range is about 1%. The average path length enhancement of the cell, due to surface texturing, is a factor of 40 [50]. Due to these absorption enhancing designs, c-Si cells have been reduced to ~ 100 μm thickness, yet they efficiently collect charge where the fundamental material absorption depth is $\sim 1,000$ μm [48]. The record c-Si solar cell is 25% efficient and commercial production cells are $\sim 22.5\%$ efficient [51]. The theoretical efficiency for these c-Si cells is $\sim 28\%$ so they are close to ideal [52]. The objective of Si NW array architectures is to achieve at least $\sim 70\%$ of the performance of these high-efficiency silicon cells, but at a much lower cost. From an optical perspective, the NW array can be designed to fulfill the functions of the antireflection coating and surface texturing while simultaneously using dramatically less silicon than a conventional cell.

11.5.1 Basic Principles of NW Array Optics

Inorganic solar cell materials have high indices of refraction, $n_s > 2.7$, and their bulk reflectivity is $\geq 30\%$. Figure 11.8 shows the reflectivity of bulk CdTe, GaAs, and c-Si as a function of wavelength. NW geometries can reduce this reflectivity substantially. For NW diameters less than the wavelength of light, the principal component of the decrease in reflectivity is due to the decrease in the effective material index. A NW array can be considered as a thin film consisting of a spatial distribution of columns (NWs) surrounded by void (refractive index = 1). The index of the NW film is determined by the index of the NW material, the volume fraction occupied by the NWs, and the alignment of the NWs with respect to the

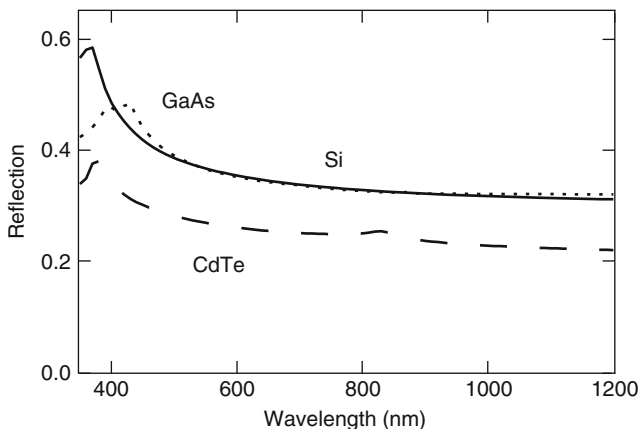


Fig. 11.8 Calculated reflection as a function of wavelength for bulk CdTe, GaAs, and crystalline Si

optical electric field. There are two limiting cases for the orientation of the NWs: parallel and perpendicular to the electric field. For perpendicular electric fields the film index, n_f , is approximately [53, 54]

$$n_f^2 = \frac{[(1-f) + (1+f)n_s^2]}{[(1+f) + (1-f)n_s^2]}, \quad (11.1)$$

where n_s is the refractive index of the semiconductor NW material and f is its volume fraction. For parallel electric fields, the index is [53, 54]

$$n_f^2 = fn_s^2 + (1-f). \quad (11.2)$$

The resulting indices as a function of volume fraction are shown in Fig. 11.9 assuming c-Si, $n_s = 3.5$. In the typical perpendicular case, the index at a volume fraction of 0.5 is only ~ 1.5 , which is considerably lower than 2.25, the linear interpolation between the two indices. This decreased index alone reduces the reflection from ~ 31 to 4%. The calculated reflection for perpendicular electric fields is shown on the right vertical axis in Fig. 11.9. Lower NW volume fractions have even lower reflection. Further decrease in the surface reflection can be achieved using tapered, conical structures in which the effective volume fraction of the solar material is negligible at the first surface (point of the cone) and gradually increases into the NW array. Because the decrease in reflection comes from a decrease in the effective index of refraction, it is relatively insensitive to the angle of incidence, particularly for NW arrays with small volume fraction.

NW array geometries and particles which scatter the light can also lead to an increase in the effective optical path length. An NW array with features comparable or smaller to the wavelength of light is a discontinuous dielectric environment which leads to light scattering and diffraction. For wavelengths that require light trapping,

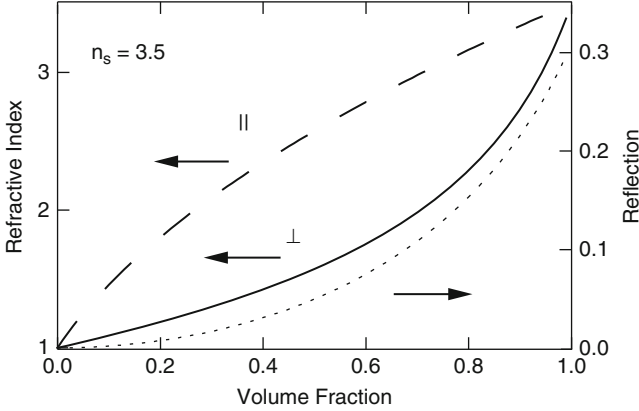


Fig. 11.9 Calculated refractive index for a thin film of columnar structures as a function of the volume fraction of columns for electric fields parallel and perpendicular to the column axis (*left vertical axis*). Calculated reflection for electric fields perpendicular to the columns (*right vertical axis*)

the NW array can be considered a weakly absorbing thin film. The basic approach to increasing the path length is to scatter light such that it propagates within the film which is then confined by total internal reflection. A widely considered ideal thin-film case is a perfectly transmissive, Lambertian (propagation direction randomized) top surface with a perfectly reflective bottom surface. In this case, the average path length is increased to

$$l = 4n_s^2d, \tag{11.3}$$

where d is the film thickness [55]. For c-Si, $n_s = 3.5$, this corresponds to a path length of $\sim 50d$. This factor of 50 enhancement is only slightly more than the factor of 40 enhancement achieved in record efficiency c-Si cells. However, typical NW arrays have structures that vary with depth into the NW film either by design or as a result of fabrication variability. They thus scatter light throughout their volume as opposed to the model case of scattering by a single Lambertian surface. Thus, even larger path length enhancements should be achievable from NW films.

The scattering efficiency (scattering cross section/particle physical cross section) of particles less than or comparable to the optical wavelength can be obtained from Rayleigh and Mie theory. The most efficient scattering size (spherical particles) occurs for

$$\pi n_s^2 D \geq 5\lambda, \tag{11.4}$$

where D is the particle diameter and λ is the optical wavelength [56]. The scattering efficiency is essentially constant above this threshold. For c-Si at 1,100 nm, the scattering is most efficient for particles $>\sim 140$ nm. The total light scattering is a product of the scattering efficiency and the number of scatterers, so the best scattering is obtained for a dense array of ~ 100 nm particles.

So far we have considered ensemble NW effects and have only required that the individual NWs have diameters less than or comparable to the wavelength of light. For NWs of this size, there are also wave guiding and resonance effects determined by the individual NW geometry and optical properties. For wavelengths comparable to the NW diameter, the NWs act as efficient energy guides for propagation along their axis and the optical modes are largely confined to the NW. The NW guided modes are strongly confined for wavelengths

$$\lambda_g \sim n_s D, \quad (11.5)$$

where D is the NW diameter [57]. For Si NWs with $n_s = 3.5$, 1, 100 nm light is strongly guided for NW diameters above ~ 300 nm. Thus for NW diameters ≥ 300 nm the NWs can act as waveguides for all wavelengths above the energy gap of Si relevant for solar cell performance. For light propagating perpendicular to the NW axis, the individual NWs also exhibit resonance effects that can alter the electric field strengths inside the wire. The resonance frequencies can be determined using the framework of leaky mode resonances [58, 59]. Silicon NWs of ~ 300 nm diameter can have resonances for optical wavelengths of $\sim 1,000$ nm. Both of these wave guiding and resonance effects can increase the electric field in the NW above that in a thin-film structure and thus increase its relative absorption. These effects are usually small compared to the combination of reduced reflection and light scattering, but it may be possible to design structures that optimize these resonances particularly to enhance absorption for wavelengths around 1,000 nm where c-Si absorption is very weak.

These basic optical effects in NW arrays imply that optical absorption will be improved most in vertical NW arrays of small diameter (~ 100 nm). The vertical orientation is best for decreasing reflection and small diameters lead to the most efficient light scattering and trapping. All of these optical effects have been included in numerical optical modeling of the NW arrays [60–63] using finite difference time domain or transfer matrix methods. Theoretical calculations generally indicate that the optical performance of the NW array is relatively insensitive to the array periodicity for spacings in the 300–1,000 nm range for small wire volume fractions < 0.3 [63].

11.5.2 Experimental Demonstrations of Increased Absorption

There has been a large amount of experimental work investigating the optical performance of NW arrays. It has been demonstrated that NW array structures, without additional antireflection coatings, can minimize reflection and increase the absorption (optical path length) [19, 28]. The best structures can have $< 1\%$ reflection and near 100% absorption throughout the 350–1,100 nm Si solar window. One example that highlights the optical efficiency of NW arrays is shown in Fig. 11.10 [28]. There the optical reflection, transmission, and absorption as a function of

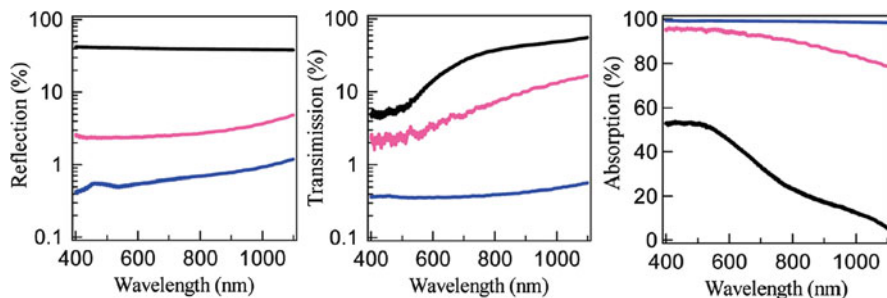


Fig. 11.10 Measured reflection (R), transmission (T), and absorption ($1-R-T$) as a function of wavelength for a nanocone array (blue), an NW array (red), and a reference thin c-Si film (black) [28]

wavelength for c-Si NW (red) and nanocone (blue) arrays and, for reference, for a $5\ \mu\text{m}$ thin c-Si film (black) is shown. The nanocones had $340\ \text{nm}$ top diameters and $800\ \text{nm}$ bottom diameters, and the NWs had $340\ \text{nm}$ diameters. The wires and cones were both $3.5\ \mu\text{m}$ long arranged in a close packed array with $800\ \text{nm}$ lattice constants and were supported on a $1.5\ \mu\text{m}$ thin c-Si film (on $2\ \mu\text{m}$ of SiO_2). The absorption was calculated from the measured reflection and transmission. The reflection from the c-Si thin film is similar to the bulk reflection shown in Fig. 11.8. This reflection is slightly larger because of the additional reflections from the c-Si/ SiO_2 and SiO_2 /Air interfaces. The reflection from the NW array varies from about 2 to 4%, consistent with the simple estimates discussed above. The nanocone array has less than 1% reflection for all wavelengths. The transmission and calculated absorption for the thin film are consistent with the c-Si optical absorption depth shown in Fig. 11.7. The absorption for both arrays is dramatically superior to the reference thin film. The nanocone array has $\sim 99\%$ absorption throughout the spectrum and the NW array has absorption ranging from ~ 95 to 80% . These structures demonstrate the extremely efficient optical absorption that can occur in nanostructured Si arrays. However, they also serve to demonstrate that optical considerations alone do not determine solar cell performance. Solar cells were fabricated using these nanocone arrays and their efficiency was only 10.8% [28], much lower than the $\sim 25\%$ implied by the optical absorption alone.

In recognition of the electrical device problems of working with small diameter NWs, some groups have focused on using relatively large (several μm) diameter wires [25, 29]. The optical performance of arrays of such large diameter wires are quite poor; they have significant surface reflection and do not dramatically increase absorption. To improve the optical performance, one group works with long ($25\text{--}50\ \mu\text{m}$) wires, coats the individual NWs with a thin film to serve as an antireflection coating, and adds $\sim 80\ \text{nm}$ diameter Al_2O_3 particles in between the wires to scatter the incoming light [25]. These techniques to improve the performance of large wire diameter arrays are consistent with the principles discussed above.

11.6 Optoelectronic Properties of Radial Nanowire Diodes

The electronic and photovoltaic properties of cylindrical NW diodes are significantly different from those of planar solar cells. These properties of p–n junction diodes can be analyzed by solving the coupled Poisson-continuity equations in order to determine depletion widths, carrier densities, and photo- and dark current densities. Analytic solutions of current densities are found by assuming that the depletion regions are free of mobile carriers, so no recombination occurs in the depletion region (depletion approximation) and that the recombination rates in the neutral regions are linear so that the photogeneration and bias factors in the continuity equations can be superimposed (superposition approximation) [5].

To gain insight into the differences in electronic properties and photovoltaic action in NW solar cells compared to planar cells, we briefly discuss solutions of Poisson’s equation to determine depletion layer widths across the radial cell, given a certain doping density. While the effects here are not important from an optical absorption perspective, they must be considered electrically to prevent total depletion of either the NW core or shell, and to evaluate the series resistances of such regions.

A radial NW diode is shown schematically in Fig. 11.11a. Here, a is the radius of the n-type NW core, N_D^+ is the ionized donor doping density on the n-side of the junction with extent r_n into the NW core, and N_A^- is the ionized acceptor doping density on the p-side of the junction with extent r_p into the NW shell. The total depletion width is $W_{nanowire} = r_p - r_n$. Within the depletion approximation, the boundary conditions for solving Poisson’s equation are (1) the electric field vanishes at both edges of the depletion region and (2) we assume $\varphi_n = V_{bi}$ and $\varphi_p = 0$, where φ is the electrostatic potential and V_{bi} is the built-in voltage. This leads to a characteristic equation for finding the shell depletion width, r_p :

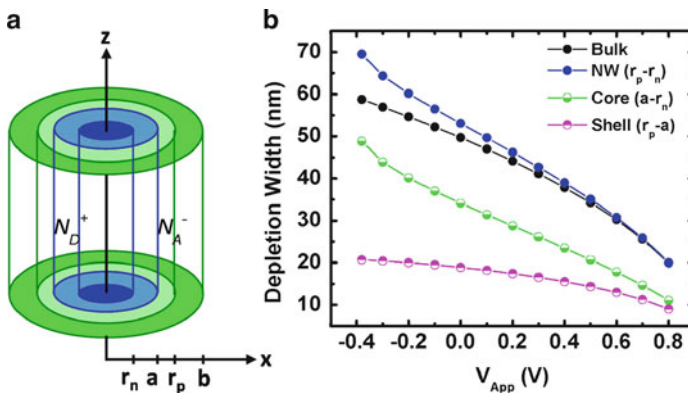


Fig. 11.11 (a) Schematic cross section of a radial NW p–n junction and (b) depletion width distribution in the core (green), shell (magenta), total depletion (blue) for a 50 nm diameter NW, compared to bulk (black), all calculated for a doping density of 10^{18} cm^{-3}

$$\begin{aligned} \frac{2\varepsilon_s V_{bi}}{qa^2} &= \frac{N_A^-}{2} \left(\frac{r_p}{a}\right)^2 \ln \left(\frac{\left(\frac{r_p}{a}\right)^2}{\frac{N_A^- + N_D^+}{N_D^+} - \frac{N_A^-}{N_D^+} \left(\frac{r_p}{a}\right)^2} \right) \\ &+ \frac{1}{2} (N_A^- + N_D^+) \ln \left(\frac{N_A^- + N_D^+}{N_D^+} - \frac{N_A^-}{N_D^+} \left(\frac{r_p}{a}\right)^2 \right), \end{aligned} \quad (11.6)$$

Where q is the electron charge and ε_s is the semiconductor dielectric constant. The charge neutrality condition on both sides of the junction gives $r_n = \sqrt{2a^2 - r_p^2}$. Figure 11.11b shows the calculated depletion widths in both the NW core and shell, and the total radial depletion width for a Si NW with a core diameter of 50 nm and doping densities of $N_D^+ = N_A^- = N = 10^{18} \text{ cm}^{-3}$ as a function of applied bias (by replacing V_{bi} with $V_{bi} - V_{App}$ in (11.6)). Also shown in Fig. 11.11b is the depletion layer width of a bulk, planar p–n junction with $N = 10^{18} \text{ cm}^{-3}$. The key difference from planar p–n junctions is that the depletion regions in the NW core and shell have different voltage dependences (the bulk junction depletion widths for planar structures would be equal and scale identically with bias). This difference is due to the increase with radius of the number of ionized charges contained in a cylindrical shell, so that for a larger radius a thinner depletion region is required to satisfy charge neutrality. As seen in Fig. 11.11b (1) the depletion region width in the NW core is larger than in the NW shell, and (2) going from forward (positive)- to reverse-bias (negative) voltages, the depletion region in the shell has a very weak dependence on applied voltage, whereas the depletion region in the core varies linearly followed by a superlinear increase just prior to total depletion, which for the example discussed here occurs at $\sim -0.4 \text{ V}$ reverse bias. Because of the strong bias dependence of the core depletion width, the total NW depletion width strongly deviates from that of the bulk at reverse biases. It is critical to keep the nondepleted NW core diameter large enough to support the solar cell photocurrent with minimal voltage loss due to its series resistance. This is easily achieved for structures with doping densities in the 10^{18} to 10^{19} cm^{-3} range and wire lengths of $\sim 5 \mu\text{m}$. In addition, for proper operation of an NW solar cell with $N = 10^{18} \text{ cm}^{-3}$ doping densities, the shell thickness has to exceed 20 nm in order to maintain p–n junction behavior and avoid Schottky contact effects on carrier extraction from the cell.

A typical Si solar cell consists of a diode formed by diffusion of n-type dopants into a thick p-type ($\sim 200 \mu\text{m}$) substrate. The n-type layer is usually heavily doped (10^{19} cm^{-3}) in order to ensure low contact and series resistances but thin enough to be transparent to incident light. The p-type layer is thick to maximize light absorption and is lightly doped ($\sim 10^{16} \text{ cm}^{-3}$) to ensure long minority electron diffusion lengths to reach the top contact. The considerations for NW solar cell design are significantly different. As discussed in the optical absorption section, arrays of small diameter NWs only $\sim 5\text{--}10 \mu\text{m}$ long are able to absorb most of the incoming solar radiation. Due to the short carrier transport length along the radial direction of the NW ($< 1 \mu\text{m}$), the minority carrier diffusion lengths do not need to be very large to achieve high quantum efficiency. This significantly lowers

the material quality required for an NW solar cell compared to conventional cells. However, surface recombination is more important in NW solar cells because the ratio of the surface area to the wire volume becomes larger as the NW diameter decreases.

To assess the influence of different device geometries and material parameters on NW solar cell performance, we need to calculate the electrical and photocurrent properties. Coupled solutions of the transport equations are generally obtained in semiconductor device simulators, and even simplified, decoupled solutions of these equations in cylindrical coordinates are generally complex and handled numerically [15]. For an intuitive perspective into NW solar cell performance, we utilize the fact that light absorption in NW arrays is essentially uniform throughout each individual NW since the absorption depth is larger than the NW diameter. We also use the cylindrical symmetry of the NW for an additional simplification to solve the 1D continuity equations that make use of depletion widths extracted from cylindrical coordinate solutions as discussed above. The boundary conditions for such solutions are well known and are applied here to the NW radial extent (Fig. 11.11a) with surface recombination boundary conditions at $r = b$ and a constant, photogenerated minority carrier density at the center of the NW. These solutions lead to the following current density equations:

$$J_{p_n} = \frac{qD_p}{L_p} \left[p_{n0} \left(e^{\frac{qV}{kT}} - 1 \right) - \frac{GL_p^2}{D_p} \right] \tanh \left(\frac{r_n}{L_p} \right), \quad (11.7)$$

$$J_{n_p} = \frac{qn_{p0} \left[D_n^2 L_n^2 \sinh \left(\frac{(b-r_p)}{L_n} \right) - D_n S L_n^3 \cosh \left(\frac{(b-r_p)}{L_n} \right) \right] \left(e^{\frac{qV}{kT}} - 1 \right)}{D_n L_n^3 \cosh \left(\frac{(b-r_p)}{L_n} \right) - S L_n^4 \sinh \left(\frac{(b-r_p)}{L_n} \right)} \quad (11.8)$$

$$+ \frac{qG S L_n^5 \cosh \left(\frac{(b-r_p)}{L_n} \right) - qG D_n L_n^4 \sinh \left(\frac{(b-r_p)}{L_n} \right) - qS G L_n^5}{D_n L_n^3 \cosh \left(\frac{(b-r_p)}{L_n} \right) - S L_n^4 \sinh \left(\frac{(b-r_p)}{L_n} \right)},$$

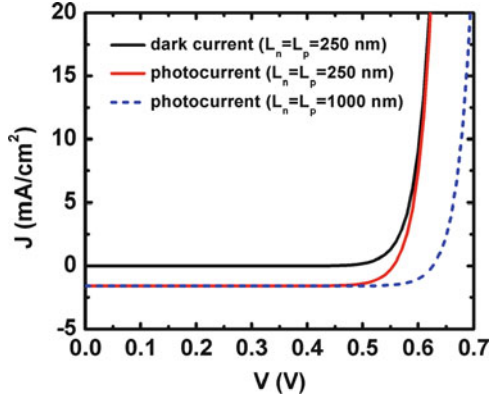
and

$$J_{\text{dep}} = -qG(r_p - r_n), \quad (11.9)$$

where J_{p_n} is the current density due to minority holes in the n-type region, J_{n_p} is the current density of minority electrons in the p-type region, and J_{dep} is the current density due to photocarrier generation in the depletion region. The optical generation rate, G , is constant throughout the NW, S is the surface recombination velocity, and V is the applied voltage. The parameters n_{p0} , p_{n0} , L_n , L_p , D_n , and D_p are the equilibrium minority electron and hole densities, minority carrier diffusion lengths, and diffusion coefficients in the p- and n-type regions, respectively.

The first parts of (11.7) and (11.8) are the dark current components of the total current densities, and their latter parts are the G-dependent photocurrent components. The photocurrent components are largely determined by the minority

Fig. 11.12 Dark and photocurrent for a single NW solar cell with $N_A = N_D = 10^{18} \text{ cm}^{-3}$ for $a = 50 \text{ nm}$, $b = 100 \text{ nm}$, and $G_L = 10^{21} \text{ cm}^{-3}$



carrier diffusion lengths. For the same NW treated in Fig. 11.11, the total current density is plotted in Fig. 11.12 for dark and light conditions and for different minority carrier diffusion lengths. Here, the minority carrier diffusion lengths considered are both larger than the neutral portions of the n- and p-type regions of the NW, so the short circuit current density, J_{sc} , does not change when the diffusion length is increased. However, the larger diffusion length does produce a $\sim 0.1 \text{ V}$ increase in the open-circuit voltage, V_{oc} , of the cell. The increase in V_{oc} is caused by the decrease in the dark current of the diode with increasing minority carrier diffusion lengths. An increase in V_{oc} with longer minority carrier diffusion lengths in NWs has been observed experimentally [29]; however, since the diameters of the Si wires used in that work were either comparable to or larger than the minority carrier diffusion lengths, J_{sc} is also increased.

The quantum efficiency, Q.E., of the device is given by

$$\text{Q.E.} = \frac{J_{sc}}{qGb} = \frac{J_{pn} + J_{np} + J_{dep}}{qGb}, \tag{11.10}$$

Figure 11.13 shows the quantum efficiency of a 100 nm diameter NW as a function of minority carrier diffusion length. Minority carrier diffusion lengths that are $\sim 2X$ the core diameter or shell thickness are sufficient to yield a Q.E. of ~ 1 . Since optical absorption can be high with NW diameters of $\sim 100 \text{ nm}$, these diffusion lengths can be significantly relaxed from that of bulk cells that require $\sim 100 \text{ }\mu\text{m}$ or more minority carrier diffusion lengths in equivalently thick Si absorption layers.

For larger diameter wires, the diffusion length must be comparable to the wire diameter to achieve high quantum efficiency. However, insertion of a thin intrinsic (undoped) absorption layer between the highly doped core/shell to create a p-i-n structure can improve the Q.E. of wires with much smaller minority carrier diffusion lengths. These effects are portrayed in Fig. 11.14 where the Q.E. is plotted against the thickness of the intrinsic layer, with fixed wire and core diameters of 500 nm and 50 nm, respectively, and for different diffusion lengths. Large minority carrier diffusion lengths produce high Q.E. at small intrinsic layer thicknesses. For small

Fig. 11.13 Quantum efficiency as function of minority carrier diffusion lengths for $N_A = N_D = 10^{18} \text{ cm}^{-3}$ for $a = 50 \text{ nm}$, $b = 100 \text{ nm}$, and $G_L = 10^{21} \text{ cm}^{-3}$, and $S = 10^3 \text{ cm/s}$

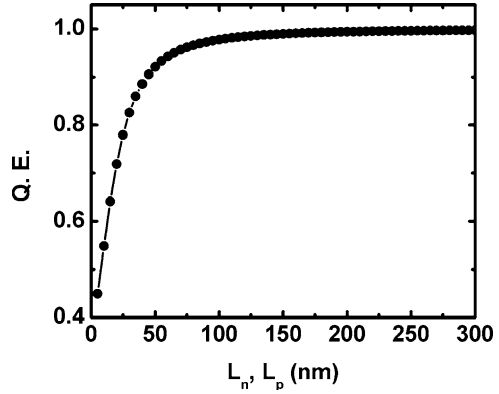
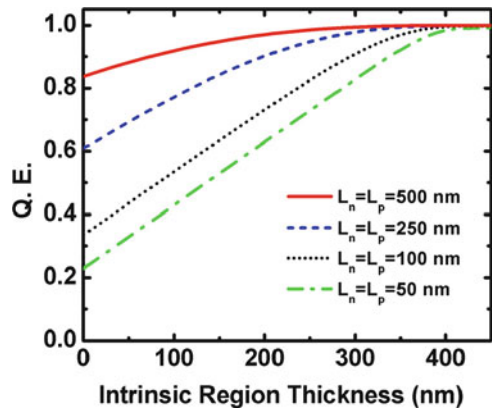


Fig. 11.14 Quantum efficiency as function of intrinsic layer thickness with different minority carrier diffusion lengths for a total NW diameter of 500 nm , $a = 50 \text{ nm}$, $N_A = N_D = 10^{18} \text{ cm}^{-3}$, $G_L = 10^{21} \text{ cm}^{-3}$, and $S = 10^3 \text{ cm/s}$



minority carrier diffusion lengths, the intrinsic layer thickness has to be increased such that the depletion current component becomes large enough to produce a high Q.E. This was observed experimentally in p-n and p-i-n core/shell NW solar cells with a few tens of nm core/intrinsic/shell thicknesses [21], indicating that minority carrier lengths are indeed short in the in situ grown polycrystalline intrinsic and n-shell layers.

11.7 Solar Cell Performance: Combined Optical and Electrical Properties

The two previous sections considered the optical properties of NW arrays and the photoelectric device properties of individual NWs. To predict the performance of an NW solar cell these properties must be combined. From an optical perspective, small diameter NWs have the best performance due to the efficiency of light scattering. Conversely, the electrical properties of large diameter NWs are superior due to the

decrease in surface recombination loss. The best solar cell performance requires a compromise between these two diverging requirements or the addition of extra optical or device elements. Two limiting cases have been considered experimentally: small diameter wires with good optical absorption and large diameter wires with good electrical performance. The best NW solar cell results to date [28] have been achieved in the previously described conical structure with optical properties shown in Fig. 11.10. Because the nanocones are of small diameter, the uniform optical absorption approach of Sect. 11.5 is appropriate. The reported cell efficiency is 10.8% with a short circuit current of 26.4 mA/cm², a V_{oc} of 0.59 V and a fill factor of 0.69. From the short circuit current, we can estimate that the photocurrent quantum efficiency of this cell is about 60% [52], assuming it is constant as a function of wavelength throughout the c-Si optical absorption region. A 60% quantum efficiency would lead to about a 15% power efficiency device if all other device parameters were ideal. The open circuit voltage is about 0.05 V smaller than ideal and the fill factor is about 0.1 too small [60]. Thus, these devices suffer from a decrease in Q.E. from the absorption implied ~ 99 to $\sim 60\%$, and from nonideal device I - V characteristics which reduce the open circuit voltage and fill factor. This structure employed 20 nm of wet oxide (SiO₂) as a surface passivation layer, which is one of the better passivation approaches. More detailed measurements of the individual nanocone performance are required to determine what properties need to be improved to increase the overall performance of these cells.

The best large diameter wire solar cell results have been achieved with 2–3 μm diameter, 45 μm long wires arranged on a square lattice with 7 μm spacing. For these large diameter wires, the optical absorption is not uniform throughout the wire and the absorption enhancement is relatively weak. The reported cell efficiency is 7.9% with a short circuit current of 24.3 mA/cm², a V_{oc} of 0.5 V and a fill factor of 0.65 [25]. From the short circuit current, we can estimate that the integrated optical absorption efficiency of this cell is about 55% [52], assuming $\sim 100\%$ internal photocurrent quantum efficiency for each wire. Surprisingly, considering that the virtue of large diameter wires is their electrical device quality, the open circuit voltage is about 0.15 V smaller than ideal and the fill factor is about 0.15 too small. This structure employed an a-SiN_x:H film as a surface passivation and antireflection layer and had 80 nm diameter Al₂O₃ particles between the wires to increase the optical scattering. Additional measurements of the individual NW performance are required to determine what properties need to be improved to increase the overall performance of these cells.

The state of the art in NW array solar cells is still at a primitive state. The above record performance efficiencies of 10.8 and 7.9% have not been confirmed by a recognized testing laboratory such as the National Renewable Energy Laboratory (NREL).¹ The solar cells were both fabricated over extremely small areas, $\sim 2.5 \times 10^{-1} \text{ cm}^2$ and $2 \times 10^{-3} \text{ cm}^2$, respectively. They are thus both smaller than the 1 cm²

¹The cell described in Yoon et al. [36] and listed as 8.7% efficient in Table 11.1 has a significant photovoltaic contribution from the substrate.

size considered the minimum required for testing of nonconcentrating solar cells [6]. Finally, there remain real questions about the areal scalability of these approaches. For NW arrays formed by VLS or etching techniques, the individual NW formation processes are largely independent and so defect occurrences must be considered. The NW arrays discussed above have pitches of $\sim 1\text{--}10\ \mu\text{m}$ corresponding to NW densities of $10^8\ \text{cm}^{-2}$ to $10^6\ \text{cm}^{-2}$. Six sigma processes require less than ~ 3.5 defects per million items produced. One thus might expect $\sim 3\text{--}300$ defective wires/cm² even with six sigma uniformity. Since the individual NW diodes are connected in parallel, one low resistance/shorting diode could ruin an entire subsection of a solar cell. It remains unclear if it is possible to achieve better than six sigma process control with the low-cost substrates and inexpensive fabrication techniques required for solar cells.

11.8 Integration Strategies for Nanowire Solar Cells

A major barrier to the mainstream adoption of Si-based PV technology is the relatively high cost associated with the materials used to manufacture individual cells, which can account for $>60\%$ of the final cost (J. Lushetsky, presented at the $\$1/W$ Workshop: ARPA-E and Office of Energy Efficiency and Renewable Energy's (EERE) Solar Energy Technology Program (SETP), Washington, DC, 2010, unpublished; [64]). For Si-based solar cell technology, a direct correlation exists between the crystalline quality of Si, the solar energy conversion efficiency, and the overall manufacturing cost. Thus, PV cells made from high-quality single-crystalline Si tend to have the highest energy conversion efficiency, and also the highest cost. One strategy to mitigate manufacturing cost is the use of lower quality material such as polycrystalline Si substrates, but at the expense of lower solar energy conversion efficiency. Integrating nanostructured materials such as Si NW arrays directly onto low-cost alternative substrates such as metal foils, glass, or polymers provides an alternative approach. This approach potentially allows a relatively high solar energy conversion efficiency provided by the single-crystalline Si NWs along with a reduction in manufacturing cost [65], as discussed in the previous sections of this chapter. Additionally, NW array growth on metal foils and polymer transfer techniques provide opportunities to reduce cost while at the same time producing solar cells that are structurally flexible and able to mechanically conform to curved surfaces such as street lights or roofing tiles.

11.8.1 General Approaches

Currently there are two basic approaches to integrating semiconductor NWs onto low-cost alternative substrates for solar cell applications. One approach is direct NW synthesis using CVD. However, the choice of an alternative substrate material

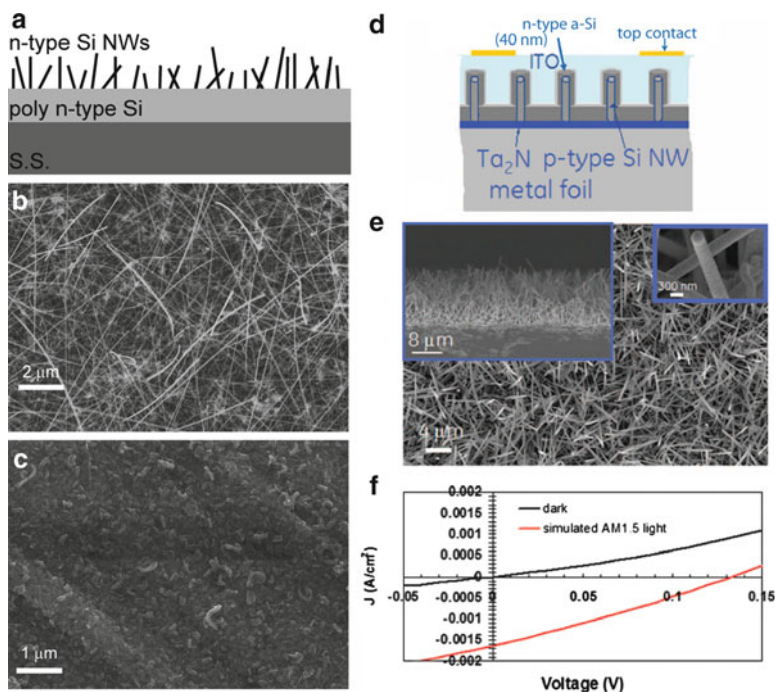


Fig. 11.15 Si NW growth on S.S. foil substrates. (a) Schematic of substrate structure. (b) SEM image of Si NWs grown on poly-Si thin film on top of S.S. (c) SEM image of silicide nanoworm formation by direct synthesis on S.S. (d) Schematic of Si NW-based solar cell on S.S. foil. (e) SEM image of Si NWs grown on Ta₂N layer on S.S. foil. (f) Dark and light current–voltage characteristics of a Si NW solar cell shown in (d). Panels (d)–(f) after [20]

is limited by the synthesis and processing requirements. Considering the typical CVD growth temperatures of $\sim 450\text{--}550^\circ\text{C}$ for Au-catalyzed VLS Si NW growth with SiH₄ and $\sim 800\text{--}1,000^\circ\text{C}$ with SiCl₄, suitable alternative substrate materials are primarily restricted to growth on metal foils such as stainless steel (S.S.) or glass substrates. Shown in Fig. 11.15a is a schematic illustrating the growth of Si nanowires on an S.S. substrate. Silicon NWs are being grown by the VLS method directly on a plasma-enhanced CVD polycrystalline Si thin-film buffer layer on S.S. (Fig. 11.15b) by the present authors. A 2 nm Au film is used as the catalyst for the NW growth. The presence of the polycrystalline Si layer served as a diffusion barrier, and also prevents unwanted silicide “nanoworm” formation (Fig. 11.15c). The thicknesses of $\sim 100\ \mu\text{m}$ (4 mil) S.S. and $\sim 400\ \text{nm}$ polycrystalline Si were optimized in order to eliminate delamination of the polycrystalline Si layer as a result of the thermal mismatch induced stresses during the NW growth.

Researchers at G.E. have demonstrated a complete Si NW-based solar cell on S.S. [20]. In their design (Fig. 11.15d), Si NWs were fabricated via VLS growth from a Au seed layer on a Ta₂N thin diffusion barrier on S.S. (Fig. 11.15e). Figure 11.15f

shows the resultant dark and light current–voltage curves. The device shows a rectifying behavior and power generation is observed; however, the authors report a low conversion efficiency of $\sim 0.1\%$ for a Si-based solar cell. Both high series and low shunt resistances appear to limit the NW solar cell efficiency and suggest the presence of a high number of parasitic short circuit paths. Similar results have also been reported by Andra et al. who demonstrated VLS Si NW growth on crystalline Si films on glass substrates (G. Andra, M. Pietsch, T. Stelzner, A. Gawlik, E. Ose, S. Christiansen, F. Falk, presented at the IEEE Photo. Spec Conf, San Diego CA, 2008, unpublished; [66]). The difficulty in obtaining good conformal coverage of thin-film overlayers on the NWs is exacerbated by the fact that NWs grown from catalyst films on polycrystalline surfaces tend to grow in a more-or-less random orientation with respect to the substrate surface. One strategy to alleviate this is by synthesis of well-defined vertical NW arrays by top-down etching techniques. Using wet electroless chemical etching, Sivakov et al. were able to synthesize a solar cell from vertical polycrystalline Si NW arrays on glass substrates which exhibited a power conversion efficiency of 4.4% [67].

Another approach to integrating NWs onto low-cost alternative substrates is by polymer transfer of NW arrays by means of a flexible polymer film with the NWs imbedded. This technique was first reported by Plass et al. where an array of VLS-grown Si wires shown in Fig. 11.16b was suspended in a PDMS film [68]. This process is depicted in Fig. 11.16a where after NW synthesis, a PDMS film was cast at the base of the array. Subsequently, a free-standing PDMS film with suspended NWs was created by mechanically peeling the film from the Si substrate. The SEM

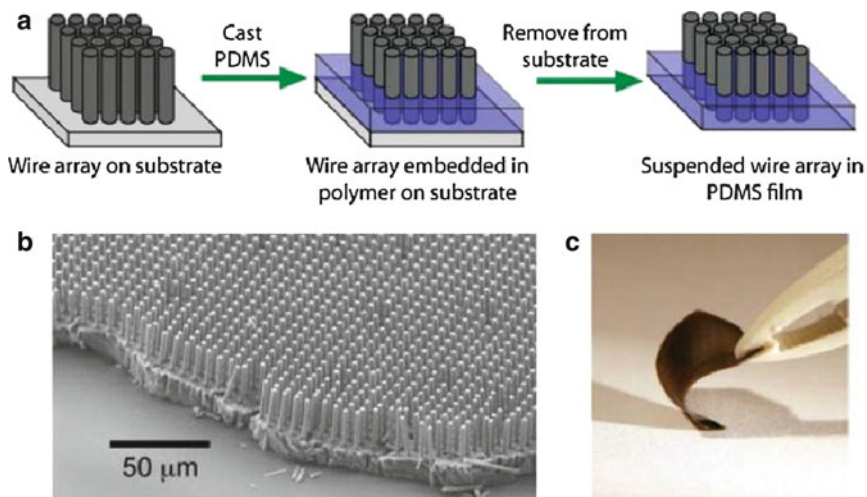


Fig. 11.16 Transfer of vertical array of Si microwires into free-standing polymer films. (a) Schematic representation of process to imbed and remove microwire array. (b) SEM image of vertical Si microwire array suspended in a PDMS film. (c) A flexible free-standing PDMS film with suspended vertical array of Si microwires. Panels (a)–(c) after [68]

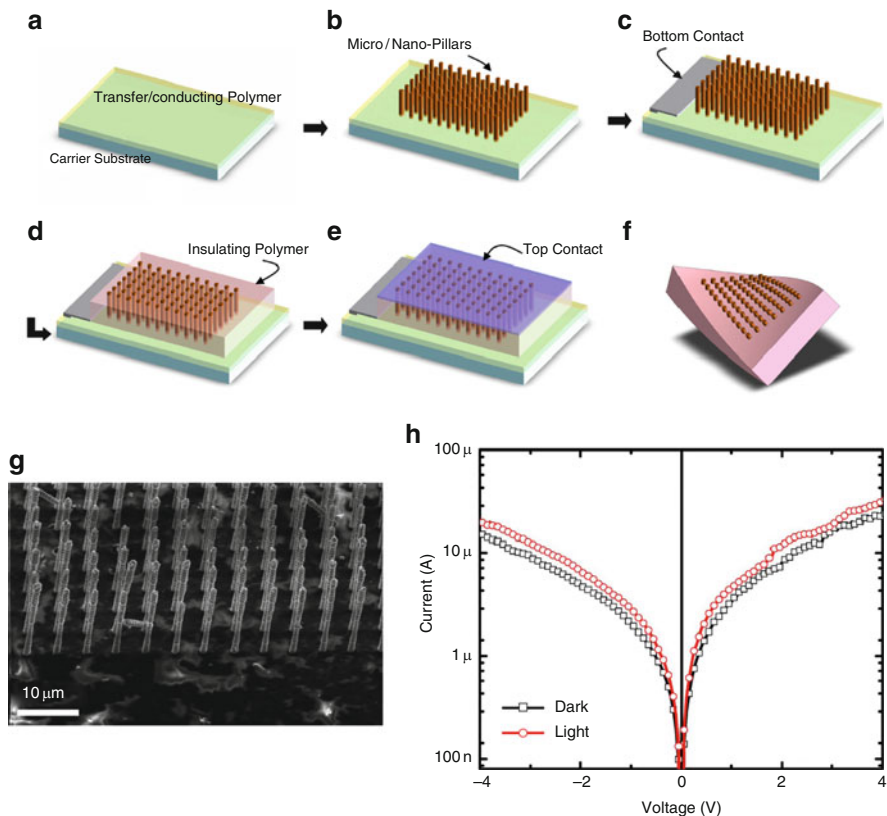


Fig. 11.17 (a) Vertical Si wire arrays are mechanically imbedded into a conducting polymer film supported on a solid substrate (e.g., glass). A lateral force is then applied to the wire substrate to shear fracture the wires, (b) leaving behind the vertical NW array imbedded in the conducting polymer. (c) A bottom contact metal is evaporated on the conducting polymer outside of the device region. (d) An insulating layer (e.g., PMMA) is infiltrated to fill the space between the wires. (e) After an etch-back step, a transparent contact (e.g., ITO) is then evaporated on top. (f) flexible Si wire array after release from carrier substrate (g) SEM image of wires imbedded in conducting polymer. (h) Electrical I - V measurement of the transferred Si nanowire photoconductor with and without optical illumination. Panels (g, h) after [71]

image in Fig. 11.16b clearly shows the vertical array of Si wires suspended in the released PDMS film. The advantage of having the NWs suspended in a polymer film is that the polymer allows a wide range of structural flexibility as demonstrated in Fig. 11.16c. Currently, there are very few reports on the performance of free-standing polymer-supported Si wire films for solar cell applications. In one report Spurgeon et al. created a photoelectrochemical cell from a polymer-supported Si wire film and demonstrated that the free-standing wire film could potentially be made into a solar cell without sacrificing solar energy conversion efficiency compared to substrate-supported NW solar cells [69].

Alternatively, a free-standing polymer-supported NW film could be fabricated by direct transfer of wire arrays into a preexisting polymer films and subsequently made into a working device [68]. This approach [70,71] is outlined in Fig. 11.17. Although the NWs were of uniform composition, the light and dark $I-V$ characteristics shown in Fig. 11.17h further demonstrate the concept of using polymer-imbedded Si wire arrays as solar cell devices.

Despite the demonstration of a range of strategies to integrate Si NWs onto low-cost alternative substrates, much work is yet to be done. For example, finding solutions to reduce the contact resistance between conducting contact layers and the Si wires is imperative to improve energy conversion efficiency and make Si NW-based solar devices competitive with existing planar technology [68].

11.9 Conclusions

Semiconducting NWs present a fascinating potential opportunity for developing high-efficiency, low-cost solar cells by decoupling light absorption and carrier separation. Significant recent advances have been made and these studies are leading to new understanding of both NW fabrication challenges and nanomaterial property control. However despite the many interesting features of NW radial p-n junction PV cells, the costs of electricity production and of PV module production remain to be determined. According to life cycle assessments of NW radial p-n junction solar cells, the electricity generation cost of NW radial p-n junction PV cells is likely to be comparable to second-generation PV cells, such as thin-film cells in Green's classification [72]. While this assessment sheds favorable light on the future of NW radial p-n junction PV cells, many challenging nanomaterials issues remain to be solved, including fundamental understanding of carrier transport, photon management, 3D architecture fabrication, and long-term device reliability.

Acknowledgements This research was funded in part by the Laboratory Directed Research and Development Program at Los Alamos National Laboratory and by the Department of Energy EERE (EB2102010) Work was performed in part at the Center for Integrated Nanotechnologies, a U.S. Department of Energy, Office of Basic Energy Sciences, user facility at Los Alamos National Laboratory (Contract DE-AC52-06NA25396).

References

1. E.C. Garnett, M.L. Brongersma, Y. Cui, M. McGehee, *Annu. Rev. Mater. Res.* DOI: [10.1146/annurev-matsci-062910--100434](https://doi.org/10.1146/annurev-matsci-062910--100434)
2. V.I. Klimov, *J. Phys. Chem. B* **110**, 16827 (2006)
3. A.J. Nozik, *Nano Lett.* **10**, 2735 (2010)
4. A. Hagfeldt, G. Boschloo, L. Sun, L. Kloo, H. Pettersson, *Chem. Rev.* **110**, 6595 (2010)
5. J. Nelson, *Physics of Solar Cells* (Imperial College Press, London, 2003)

6. M.A. Green, K. Emery, Y. Hishikawa, W. Warta, *Prog. Photovolt.* **19**, 84 (2011)
7. C.A. Wolden, J. Kurtin, J.B. Baxter, I. Repins, S.E. Shaheen, J.T. Torvik, A.A. Rockett, J.M. Fthenakis, E.S. Aydil, *J. Vac. Sci. Technol. A* **29**, 030801 (2011)
8. <http://www.nrel.gov/analysis/sam/>
9. M.A. Green, S.R. Wenham, *Appl. Phys. Lett.* **65**, 2907 (1994)
10. K.J. Weber, A.W. Blakers, M.J. Stocks, J.H. Babaei, V.A. Everett, A.J. Neuendorf, P.J. Verlinden, *IEEE Electron Dev. Lett.* **25**, 37 (2004)
11. R.S. Wagner, W.C. Ellis, *Appl. Phys. Lett.* **4**, 89 (1964)
12. S.T. Picraux, S.A. Dayeh, P. Manandhar, D.E. Perea, S.G. Choi, *JOM* **62**, 35 (2010)
13. C.E. Kendrick, H.P. Yoon, Y.A. Yuwen, G.D. Barber, H.T. Shen, T.E. Mallouk, E.C. Dickey, T.S. Mayer, J.M. Redwing, *Appl. Phys. Lett.* **97**, 143108 (2010)
14. B.M. Kayes, M.A. Filler, M.C. Putnam, M.D. Kelzenberg, N.S. Lewis, H.A. Atwater, *Appl. Phys. Lett.* **91**, 103110 (2007)
15. B.M. Kayes, H.A. Atwater, N.S. Lewis, *J. Appl. Phys.* **97**, 114302 (2005)
16. L. Hu, G. Chen, *Nano Lett.* **7**, 3249 (2007)
17. J. Zhu, Z.F. Yu, G.F. Burkhard, C.M. Hsu, S.T. Connor, Y.Q. Xu, Q. Wang, M. McGehee, S.H. Fan, Y. Cui, *Nano Lett.* **9**, 279 (2009)
18. Z.Y. Fan, R. Kapadia, P.W. Leu, X.B. Zhang, Y.L. Chueh, K. Takei, K. Yu, A. Jamshidi, A.A. Rathore, D.J. Ruebusch, M. Wu, A. Javey, *Nano Lett.* **10**, 3823 (2010)
19. E. Garnett, P.D. Yang, *Nano Lett.* **10**, 1082 (2010)
20. L. Tsakalakos, J. Balch, J. Fronheiser, B.A. Korevaar, O. Sulima, J. Rand, *Appl. Phys. Lett.* **91**, 23317 (2007)
21. B. Tian, X.L. Zheng, T.J. Kempa, Y.J. Fang, N. Yu, G. Yu, J. Huang, C.M. Lieber, *Nature* **449**, 885–890 (2007)
22. L.W. Yu, B. O'Donnell, P.J. Alet, P.R.I. Cabarrocas, *Solar Energy Mater. Solar Cells* **94**, 1855 (2010)
23. O. Gunawan, S. Guha, *Solar Energy Mater. Solar Cells* **93**, 1388 (2009)
24. C.E. Kendrick, S.M. Eichfeld, Y. Ke, X.J. Weng, X. Wang, T.S. Mayer, J.M. Redwing, *Proc. SPIE* **7768**, 77680I (2010)
25. M.C. Putnam, S.W. Boettcher, M.D. Kelzenberg, D.B. Turner-Evans, J.M. Spurgeon, E.L. Warren, R.M. Briggs, N.S. Lewis, H.A. Atwater, *Energy Environ. Sci.*, **3**, 1037 (2010)
26. M.D. Kelzenberg, D.B. Turner-Evans, M.C. Putnam, S.W. Boettcher, R.M. Briggs, J.Y. Baek, N.S. Lewis, H.A. Atwater, *Energy Environ. Sci.* **4**, 866 (2011)
27. M.J. Naughton, K. Kempa, Z.F. Ren, Y. Gao, J. Rybczynski, N. Argenti, W. Gao, Y. Wang, Y. Peng, J.R. Naughton, G. McMahon, T. Paudel, Y.C. Lan, M.J. Burns, A. Shepard, M. Clary, C. Ballif, F.J. Haug, T. Soderstrom, O. Cubero, C. Eminian, *Phys. Status Solidi – RRL* **4**, 181 (2010)
28. Y.R. Lu, A. Lal, *Nano Lett.* **10**, 4651 (2010)
29. H.P. Yoon, Y.A. Yuwen, C.E. Kendrick, G.D. Barber, N. Podraza, J.M. Redwing, T.E. Mallouk, C.R. Wronski, T.S. Mayer, *Appl. Phys. Lett.* **96**, 213503 (2010)
30. E.C. Garnett, P.D. Yang, *J. Am. Chem. Soc.* **130**, 9224 (2008)
31. J.Y. Jung, Z. Guo, S.W. Jee, H.D. Um, K.T. Park, M.S. Hyun, J.M. Yang, J.H. Lee, *Nanotechnology* **21**, 445303 (2010)
32. X. Wang, K.L. Pey, C.H. Yip, E.A. Fitzgerald, D.A. Antoniadis, *J. Appl. Phys.* **108**, 124303 (2010)
33. J.A. Czaban, D.A. Thompson, R.R. LaPierre, *Nano Lett.* **9**, 148 (2009)
34. C. Colombo, M. Heiss, M. Gratzel, A.F.I. Morral, *Appl. Phys. Lett.* **94**, 173108 (2009)
35. N. Tajik, Z. Peng, P. Kuyanov, R.R. LaPierre, *Nanotechnology* **22**, 225402 (2011)
36. Y. Dong, B. Tian, T.J. Kempa, C.M. Lieber, *Nano Lett.* **9**, 2183 (2009)
37. K.P. Musselman, A. Wisnet, D.C. Iza, H.C. Hesse, C. Scheu, J.L. MacManus-Driscoll, L. Schmidt-Mende, *Adv. Mater.* **22**, E254 (2011)
38. B.D. Yuhas, P.D. Yang, *J. Am. Chem. Soc.* **131**, 3756 (2009)

39. Z. Fan, H. Razavi, J.-w. Do, A. Moriwaki, O. Ergen, Y.-L. Chueh, P.W. Leu, J.C. Ho, T. Takahashi, L.A. Reichertz, S. Neale, K. Yu, M. Wu, J.W. Ager, A. Javey, *Nat. Mater.* **8**, 648 (2009)
40. P. Liu, V.P. Singh, C.A. Jarro, S. Rajaputra, *Nanotechnology* **22**, 145304 (2011)
41. D. Li, C.-J. Chien, S. Deora, P.-C. Chang, E. Moulin, J.G. Lu, *Chem. Phys. Lett.* **501**, 446 (2011)
42. A.A.D.T. Damitha, D.M.N.M. Dissanayake, S.R.P. Silva, *IEEE J. Sel. Topics Quantum Electron.* **16**, 1595 (2010)
43. Q. Zhang, G. Cao, *Nano Today* **6**, 91 (2011)
44. J.E. Allen, E.R. Hemesath, D.E. Perea, J.L. Lensch-Falk, J.Y. Li, F. Yin, M.H. Gass, P. Wang, A.L. Bleloch, R.E. Palmer, L.J. Lauhon, *Nat. Nanotechnol.* **3**, 168 (2008)
45. M.D. Kelzenberg, D.B. Turner-Evans, B.M. Kayes, M.A. Filler, M.C. Putnam, N.S. Lewis, H.A. Atwater, *Nano Lett.* **8**, 710 (2008)
46. Y. Gu, J.P. Romankiewicz, J.K. David, J.L. Lensch, L.J. Lauhon, *Nano Lett.* **6**, 948 (2006)
47. www.ioffe.rssi.ru/SVA/NSM
48. M.A. Green, *Semicond. Sci. Technol.* **8**, 1 (1993)
49. J. Zhao, M.A. Green, *IEEE Trans. Electron Dev.* **38**, 1925 (1991)
50. J. Zhao, A. Wang, P. Altermatt, M.A. Green, *Appl. Phys. Lett.* **66**, 3636 (1995)
51. (2011–12–5)
52. S.M. Sze, *Physics of Semiconductor Devices*, 2nd edn. (John Wiley & Sons, New York, NY, 1981)
53. M. Harris, H.A. Macleod, S. Ogura, *Thin Solid Films* **57**, 173 (1979)
54. H.A. Macleod, *J. Vac. Sci. Technol. A* **4**, 418 (1986)
55. P. Campbell, M.A. Green, *J. Appl. Phys.* **62**, 243 (1987)
56. A.J. Cox, A.J. DeWeerd, J. Linden, *Am. J. Phys.* **70**, 620 (2002)
57. L. Tong, J. Lou, E. Mazur, *Opt. Express* **12**, 1025 (2004)
58. W.F. Liu, J.I. Oh, W.Z. Shen, *IEEE Electron Dev. Lett.* **32**, 45 (2011)
59. L. Cao, J.S. White, J.-S. Park, J.A. Schuller, B.M. Clemens, M.L. Brongersma, *Nat. Mater.* **8**, 643 (2009)
60. M.D. Kelzenberg, M.C. Putnam, D.B. Turner-Evans, N.S. Lewis, H.A. Atwater, in *Proceedings of the 34th IEEE PVSC, USC 1948* (2009)
61. H. Bao, X. Ruan, *Opt. Lett.* **35**, 3378 (2010)
62. C. Lin, M.L. Povinelli, *Opt. Express* **17**, 19371 (2009)
63. J. Li, H.Y. Yu, S.M. Wong, X. Li, G. Zhang, P.G.-Q. Lo, D.-L. Kwong, *Appl. Phys. Lett.* **95**, 243113 (2009)
64. H.M. Lee, *Phys. High Technol. (Korean Phys. Soc.)* **17**, 15 (2008)
65. N.S. Lewis, *Science* **315**, 798 (2007)
66. T. Stelzner, M. Pietsch, G. Andra, F. Falk, E. Ose, S. Christiansen, *Nanotechnology* **19**, 295203 (2008)
67. V. Sivakov, G. Andra, A. Gawlik, A. Berger, J. Plentz, F. Falk, S.H. Christiansen, *Nano Lett.* **9**, 1549 (2009)
68. K.E. Plass, M.A. Filler, J.M. Spurgeon, B.M. Kayes, S. Maldonado, B.S. Brunschwig, H.A. Atwater, N.S. Lewis, *Adv. Mater.* **21**, 325 (2009)
69. J.M. Spurgeon, S.W. Boettcher, M.D. Kelzenberg, B.S. Brunschwig, H.A. Atwater, N.S. Lewis, *Adv. Mater.* **22**, 3277 (2010)
70. V.J. Logeeswaran, A.M. Katzenmeyer, M.S. Islam, *IEEE Trans Electron Dev.* **57**, 1856 (2010)
71. V.J. Logeeswaran, M. Ombaba, A.M. Katzenmeyer, M. S. Islam, *Energy harvesting and storage: Materials, devices, and applications. Proc. SPIE* **7683**, 768313 (2010)
72. M.A. Green, *Prog. Photovolt.* **9**, 123–135 (2001)